Progress In Electromagnetics Research, PIER 81, 413–436, 2008

SPM NUMERICAL RESULTS FROM AN EFFECTIVE SURFACE IMPEDANCE FOR A ONE-DIMENSIONAL PERFECTLY-CONDUCTING ROUGH SEA SURFACE

Y. Brelet and C. Bourlier

Institut de Recherche en Electrotechnique
et Electronique de Nantes Atlantique (IREENA)
Ecole Polytechnique de l'Université de Nantes
La Chantrerie, Rue Christian Pauc, BP 50609
44036 Nantes Cedex 3, France

Abstract—From the analytical theory of rough surface Green's function based on the extension of the diagram method of Bass, Fuks and Itô, with the smoothing approximation, numerical results are presented for Gaussian and sea spectra and compared with a benchmark method by considering a one-dimensional perfectly conducting Gaussian rough surface. The effects of multiple scattering due to the surface roughness are incorporated systematically into the solutions through an effective surface impedance, which can be iterated up to the second-order. In addition, comparisons of the bistatic scattering coefficients are presented with the first- and second- orders conventional small perturbation method. This study will be useful for remote sensing of the ocean surface, especially when the transmitter is close to the surface.

1. INTRODUCTION

The scattering of waves from rough surfaces has been investigated using a variety of asymptotic mathematical formulations [1–9]. The most popular are the Small Perturbation Method (SPM) and the Kirchhoff Approximation (KA). For example, the Kirchoff approximation requires that the incident wavelength be much smaller than the radius of curvature of the surface. In contrast, the Small Perturbation Method exploits the smallness of the roughness amplitude to generate an expression for the scattered field. It expands the phase term of the exponential of the field in a power series in surface heights, comparatively to the wavelength [2, 6, 7]. More recently, to improve

this scheme, the SPM has been derived using Green's formulation. We can quote for a one dimensional Perfectly Conducting (PC) surface, the works of Bass *et al.* [10] and Ishimaru *et al.* [11]. These authors based their works on the original published paper of Feinberg [12]. Comparatively to classical SPM, the extended SPM allows to take into account, via the introduction of an effective surface impedance, the multiple scattering of the first-order development. In the paper of Fuks, only mathematical development is presented. Those of Ishimaru [11] and Itô [13] shown only numerical results for a Gaussian spectrum with Gaussian statistics. In this paper, we propose to compare the Extended Small Perturbation Method to a benchmark method, based on the Method of Moments, for a perfectly conducting (H and V polarizations) rough sea surface obeying to the Elfouhaily *et al.* spectrum [14], in HF-VHF band. Moreover, comparisons of the second-order surface impedance and the reflection coefficient, obtained in term of the surface impedance, are made between Gaussian and sea spectra. Finally, we present some comparisons of the bistatic scattering coefficient between the first- and the second-orders conventional SPM, the extended SPM and the benchmark method (based on the Method of Moments) for Gaussian and sea spectra.

2. MATHEMATICAL FORMULATION OF THE PROBLEM

2.1. Introduction

We consider a one-dimensional perfectly conducting rough surface. The field at observation point consists of the coherent and the incoherent fields. The coherent field propagates over the flat surface with the equivalent reflection coefficient, which includes the effects of rough surface scattering. As the coherent field propagates over the rough surface, the field eventually diminishes and a part of the field is gradually converted into the incoherent (diffuse) field.

From the first order solution of the alternative approach summarized in this paper, a correction of the SPM of Rice is obtained. The correction gives a physical interpretation to the interaction which results from multiple scattering in such random rough surfaces. The Green's function method leads to average integral equations of the scattered waves. From the nonlinear Dyson and Bethe-Salpeter equations, the first two moments of the Green's function are derived. Since the surface is Dirichlet or Neumann, the equivalent impedance is zero for the flat surface, whereas the impedance is not zero due to the presence of roughness.

2.2. Basic Problem

Consider the scattering of scalar waves from a random rough surface described by $z = \zeta(x)$. The geometry is illustrated in Fig. 1.

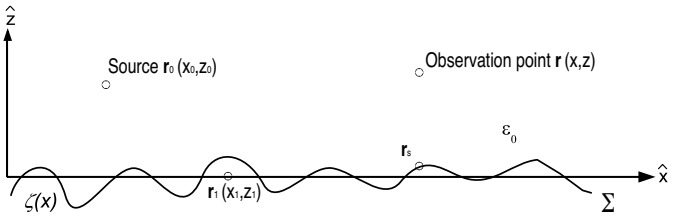

Figure 1. The rough surface is described by $z = \zeta(x)$. The source point is at $\mathbf{r}_0$, the observation point is at $\mathbf{r}$ and $\mathbf{r}_1$ is on the flat surface at $z = 0$. The surface is assumed to be infinite in $\hat{x}$ direction, and invariant along $\hat{y}$ direction (1D surface).

The incident plane wave upon the rough surface has a wave vector $\mathbf{k}_0 = \kappa\hat{\mathbf{x}} + k_z(\kappa)\hat{\mathbf{z}}$, with

$$k_z(\kappa) = \begin{cases} \sqrt{k_0^2 - \kappa^2} & \text{for } \kappa \le k_0 \\ i\sqrt{\kappa^2 - k_0^2} & \text{for } \kappa > k_0 \end{cases}$$

We let $\mathbf{r}_s = (x, \zeta(x))$ be a point on the rough surface. The surface height defined with respect to the $z = 0$ plane is assumed to be statistically homogeneous and obeys a Gaussian process characterized by:

$$\langle \zeta(\mathbf{r}) \rangle = 0 \qquad \langle \zeta(\mathbf{r}_1)\zeta(\mathbf{r}_2) \rangle = \Gamma(\mathbf{r}_1 - \mathbf{r}_2) \tag{1}$$

where the operator $\langle \bullet \rangle$ denotes the statistical average. $\Gamma(\mathbf{r}_1 - \mathbf{r}_2)$ is the surface height correlation function defined from the spectral density $\tilde{W}(\kappa)$ (height spectrum) as

$$\Gamma(\mathbf{r}_1 - \mathbf{r}_2) = \frac{1}{2\pi} \int \mathrm{d}\kappa \tilde{W}(\kappa) e^{i\kappa(\mathbf{r}_1 - \mathbf{r}_2)} \tag{2}$$

2.3. Equivalent Boundary Condition for TE and TM

This subsection gives briefly the equations needed for simulations [3]. The Green's function for a given point source located at $\mathbf{r} = \mathbf{r}_0$ satisfies the equation

$$(\nabla^2 + k_0^2) G_p(\mathbf{r}, \mathbf{r}_0) = -\delta(\mathbf{r} - \mathbf{r}_0) \qquad p = h \quad \text{or} \quad v \tag{3}$$

with the following boundary condition

$$G_h(\mathbf{r},\mathbf{r}_0)=0 \qquad \text{Dirichlet} \qquad \mathbf{r}=\mathbf{r}_s\in\Sigma \tag{4}$$

or

$$\frac{\partial G_v(\mathbf{r},\mathbf{r}_0)}{\partial n}=0 \qquad \text{Neumann} \qquad \mathbf{r}=\mathbf{r}_s\in\Sigma \tag{5}$$

where k_0 is the wave number in free space, and $\hat{n}$ is the unit vector normal to the perturbed surface. The subscripts $p=h$ and $p=v$ refer to waves subject to the Dirichlet and the Neumann boundary conditions, respectively. We consider a slightly rough random surface, for which $|k_0\zeta\cos\theta_i|<1$ and $|\partial\zeta/\partial x|<1$ [5], where θ_i is the angle of incidence of a plane wave. We write an equivalent boundary condition at $z=0$ by expanding the Green's function in (4) and (5) about the surface height $\zeta(x)$ and include the first powers in ζ. We then obtain

$$\frac{\partial}{\partial n}=\frac{-\dfrac{\partial\zeta}{\partial x}\dfrac{\partial}{\partial x}+\dfrac{\partial}{\partial z}}{\left(1+\left(\dfrac{\partial\zeta}{\partial x}\right)^2\right)^{1/2}}\approx-\frac{\partial\zeta}{\partial x}\frac{\partial}{\partial x}+\frac{\partial}{\partial z}+\cdots \tag{6}$$

since we have assumed earlier that $|\partial\zeta/\partial x|\ll 1$, the denominator is ≈ 1. In addition, we use the following Taylor expansion of the Green's function about $z=0$

$$G_p(\mathbf{r}_1)+\zeta(x_1)\frac{\partial}{\partial z_1}G_p(\mathbf{r}_1)+\frac{\zeta^2(x_1)}{2}\frac{\partial^2}{\partial z_1^2}G_p(\mathbf{r}_1)\cdots \tag{7}$$

where $\mathbf{r}_1$ is on the flat surface at $z=0$. By keeping only the first-order term in ζ, the boundary conditions of (4) and (5) for respectively Dirichlet and Neumann boundary conditions, become for the first-order

$$G_h+\zeta_1\frac{\partial}{\partial z_1}G_h=0 \tag{8}$$

$$-\frac{\partial\zeta_1}{\partial x_1}\frac{\partial}{\partial x_1}G_v+\frac{\partial}{\partial z_1}G_v+\zeta_1\frac{\partial^2}{\partial z_1^2}G_v=0 \tag{9}$$

We now make use of the Green's Theorem

$$\begin{aligned}G(\mathbf{r},\mathbf{r}_0) \;=\; & G_0(\mathbf{r},\mathbf{r}_0)+\int_\Sigma \mathrm{d}\mathbf{r}_1\left[G(\mathbf{r},\mathbf{r}_1)\frac{\partial}{\partial n_1}G_0(\mathbf{r}_1,\mathbf{r}_0)\right.\\ & \left.-G_0(\mathbf{r},\mathbf{r}_1)\frac{\partial}{\partial n_1}G(\mathbf{r}_1,\mathbf{r}_0)\right]\end{aligned} \tag{10}$$

where G_0 is the flat-surface Green's function satisfying boundary condition at $z = 0$. Applying it to the half-space above the average surface along with equivalent boundary conditions (7) and making use of the flat-surface Green's function and its boundary condition, yields to the following integral equation for the Green's function

$$G_p(\mathbf{r}, \mathbf{r}_0) = G_p^0(\mathbf{r}, \mathbf{r}_0) + \int_{\Sigma=0} \mathrm{d}\mathbf{r}_1 G_p^0(\mathbf{r}, \mathbf{r}_1) V_p(\zeta(x_1)) G_p(\mathbf{r}_1, \mathbf{r}_0) \quad (11)$$

where we define

$$V_p(\zeta(x_1)) = -\frac{\partial^{\leftarrow}}{\partial z_1}\zeta(x_1)\frac{\partial^{\rightarrow}}{\partial z_1} \qquad p = h \quad (12)$$

$$V_p(\zeta(x_1)) = -\zeta(x_1)\left(\frac{\partial^{\leftarrow}}{\partial x_1}\hat{x} - \frac{\partial^{\rightarrow}}{\partial z_1}\hat{z}\right).\nabla_{\mathbf{r}_1} \qquad p = v \quad (13)$$

$V_p(\zeta(x_1))$ is defined as the random surface potential, which is a function of the random surface height $\zeta(x)$. Here, the integration in (11) is over the entire $z = 0$ plane, and G_p^0 is the known Green's function satisfying boundary condition on the unperturbed surface and is not the free space Green's function. In (13), the attached subscript $\mathbf{r}_1$ of $\nabla_{\mathbf{r}_1}$ designates differentiation with respect to the point $(x_1, \zeta(x_1))$. Also, the arrows on the derivatives indicate the direction in which the derivatives are operated. For example, in (12), the left-derivative will operate leftward, making differentiation of $G_p^0(\mathbf{r}, \mathbf{r}_1)$ with respect to z_1, and in (13), the left-derivative will operate his differentiation with respect to x_1 over the function $\zeta(x_1)$.

2.4. Reflection Coefficient for Coherent Waves

Starting with the integral Eq. (11), we can obtain the fundamental Dyson equation used to describe the rough surface Green's function. The detailed derivation of Dyson equation using the diagram method is given in [3, 15]. This a nonlinear equation for the coherent (average) Green's function $\langle G \rangle$. To simplify the problem, a first-order smoothing operation is applied to Dyson equation making it linear.

The nonlinear Dyson's equation for the coherent Green's function is then,

$$\langle G_p(\mathbf{r}, \mathbf{r}_0)\rangle = G_p^0(\mathbf{r}, \mathbf{r}_0) + \int \mathrm{d}\mathbf{r}_1 \mathrm{d}\mathbf{r}_2 G_p^0(\mathbf{r}, \mathbf{r}_2)\mathcal{M}(\mathbf{r}_1, \mathbf{r}_2)\langle G_p(\mathbf{r}_1, \mathbf{r}_0)\rangle \quad (14)$$

$\mathcal{M}(\mathbf{r}_1, \mathbf{r}_2)$ is the so-called Mass operator. Note that Eq. (14) applies to any point $\mathbf{r}$ above the surface $z = 0$. As $\mathbf{r}$ approaches the flat

surface, $G_p^0(\mathbf{r},\mathbf{r}_0)$ becomes zero, but $G_p^0(\mathbf{r},\mathbf{r}_0)$ inside the integral is not zero because $\mathcal{M}$ includes the derivative $\partial/\partial z$. In addition, note that $\langle G_p(\mathbf{r},\mathbf{r}_0)\rangle$ is not zero on the flat surface.

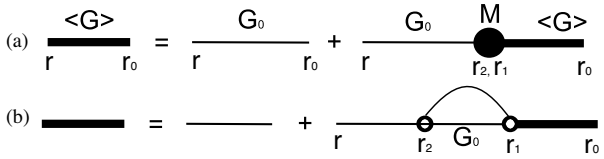

Figure 2. (a) Diagrammatic form for the nonlinear Dyson's equation for the coherent Green's function. (b) Dyson's equation with the smoothing approximation.

To simplify the Dyson equation, the Mass operator may be approximated using the first-order smoothing operation. Fig. 2 shows Dyson equation using the first-order smoothing in diagrammatic form, where the flat-surface Green's function G_p^0 is the solid line, and the mean Green's function $\langle G_p\rangle$ is the bold solid line. We can write the Mass operator under this approximation, for both Dirichlet and Neumann boundary conditions

$$\mathcal{M}(\mathbf{r}_1,\mathbf{r}_2) = \langle V_p(\zeta(x_1))G_p^0(\mathbf{r}_2,\mathbf{r}_1)V_p(\zeta(x_2))\rangle \tag{15}$$

The variables z_1 and z_2 in the Green's function are put equal to zero once the differentiation is carried out, since the Green's theorem in (10) has been simplified by derivating an approximate equivalent boundary condition at $z = 0$, giving (11). To solve Dyson equation for the coherent Green's function, we make use of a spatial Fourier transform representation

$$\langle G_p(\mathbf{r},\mathbf{r}_0)\rangle = \frac{1}{2\pi}\int \mathrm{d}\kappa \langle G_p(\kappa,z,z_0)\rangle e^{i\kappa(\mathbf{r}-\mathbf{r}_0)} \tag{16}$$

where the spatial Fourier transform $\langle G_p(\kappa,z,z_0)\rangle$ of the coherent Green's function $\langle G_p(\mathbf{r},\mathbf{r}_0)\rangle$ satisfying the boundary condition and the radiation condition at $z=\infty$ is given by

$$\langle G_p(\kappa,z,z_0)\rangle = \frac{i}{2k_z(\kappa)}\left[e^{ik_z(\kappa)|z-z_0|} + \mathcal{R}_p(\kappa)e^{ik_z(\kappa)(z+z_0)}\right] \tag{17}$$

with, for the flat-surface Green's function $G_p^0(\mathbf{r},\mathbf{r}_0)$, $\mathcal{R}_h(\kappa) = -1$ in Dirichlet case and $\mathcal{R}_v(\kappa) = +1$ in Neumann case. After some cumbersome manipulations from (14) and (15), along with (16) and (17), we arrive at the following first-order reflexion coefficient for

Dirichlet and Neumann boundary conditions, respectively

$$\mathcal{R}_{h1}(\kappa) = \frac{k_z(\kappa)Z_{h1}(\kappa) - k_0}{k_z(\kappa)Z_{h1}(\kappa) + k_0} \tag{18}$$

$$\mathcal{R}_{v1}(\kappa) = \frac{k_z(\kappa) - k_0 Z_{v1}(\kappa)}{k_z(\kappa) + k_0 Z_{v1}(\kappa)} \tag{19}$$

where

$$Z_{h1}(\kappa) = \int \mathrm{d}\kappa' k_z(\kappa')\tilde{W}(\kappa - \kappa') \tag{20}$$

$$Z_{v1}(\kappa) = \int \frac{\mathrm{d}\kappa'}{k_0 k_z(\kappa')}(k_0^2 - \kappa\kappa')^2\tilde{W}(\kappa - \kappa') \tag{21}$$

which is consistent with Fuks et al. [7].

The integrand in (21) exhibits a pole $k_z(p)$. We shall discuss the evaluation of this pole in Appendix A.

The nonlinear Dyson equation enables us to obtain solutions which are consistent with the energy conservation requirement [16] and account for multiple scattering to a still higher order. By repeating the procedure to the 2nd iteration solution [17], we can write the effective surface impedance at the second order

$$Z_{h2}(\kappa) = \int \mathrm{d}\kappa' \frac{k_z(\kappa')k_0}{k_0 + k_z(\kappa')Z_{h1}(\kappa')}\tilde{W}(\kappa - \kappa') \tag{22}$$

$$Z_{v2}(\kappa) = \int \mathrm{d}\kappa' \frac{(k_0^2 - \kappa\kappa')^2}{k_0[k_z(\kappa') + k_0 Z_{v1}(\kappa')]}\tilde{W}(\kappa - \kappa') \tag{23}$$

2.5. Incoherent Intensity

Let us now consider the second moment of the field, or the incoherent intensity. For small surface roughness, the coherent field will dominate. However, as the roughness increases, the coherent field diminishes, and the incoherent intensity becomes dominant. The incoherent intensity is obtained from the Bethe-Salpeter equation, which describes the correlation of fields at $\mathbf{r}$ and $\mathbf{r}'$ due to the sources located at $\mathbf{r}_0$ and $\mathbf{r}_0'$. The Bethe-Salpeter equation which will yield the integral equation describing the second moment of the Green's function is given by the relation

$$\Gamma_p(\mathbf{r}, \mathbf{r}_0, \mathbf{r}', \mathbf{r}_0') = \langle G_p(\mathbf{r}, \mathbf{r}_0)G_p^*(\mathbf{r}', \mathbf{r}_0')\rangle = \Gamma_{coh} + \Gamma_{incoh} \tag{24}$$

where $\Gamma_{coh} = \langle G_p(\mathbf{r}, \mathbf{r}_0)\rangle\langle G_p^*(\mathbf{r}', \mathbf{r}_0')\rangle$ is the coherent intensity and Γ_{incoh} is the incoherent or fluctuating intensity or diffuse component.

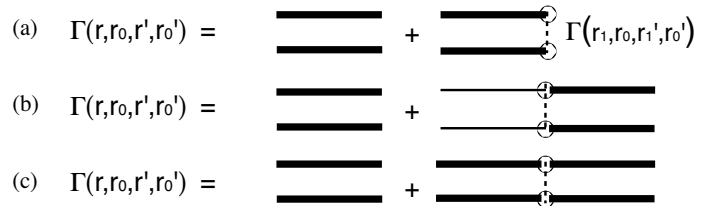

Figure 3. Diagrammatic forms of (a) Bethe-Salpeter equation via the first-order smoothing approximation [15], (b) Ishimaru's Bethe-Salpeter equation with the first-order smoothing approximation [11], (c) Itô's first-order Bethe-Salpeter equation [13].

In Fig. 3, a diagrammatic representation of the Bethe-Salpeter equation describing the second moment of the Green's function for the covariance of the field in using the *first-order smoothing approximation* [15] is displayed.

$$\langle G_p(\mathbf{r},\mathbf{r}_0)G_p^*(\mathbf{r}',\mathbf{r}_0')\rangle = \langle G_p(\mathbf{r},\mathbf{r}_0)\rangle\langle G_p^*(\mathbf{r}',\mathbf{r}_0')\rangle + \int \mathrm{d}\mathbf{r}_1\mathbf{r}_1'\langle G_p(\mathbf{r},\mathbf{r}_1)\rangle$$
$$\times\langle G_p^*(\mathbf{r}',\mathbf{r}_1')\rangle\langle V_p(\zeta(x_1))V_p(\zeta(x_1'))\rangle\langle G_p(\mathbf{r}_1,\mathbf{r}_0)G_p^*(\mathbf{r}_1',\mathbf{r}_0')\rangle \tag{25}$$

where the term in the integral, representing the incoherent intensity, can be rewritten, at the first order iteration shown in Fig. 3, as:

$$\langle G_p(\mathbf{r},\mathbf{r}_0)G_p^*(\mathbf{r}',\mathbf{r}_0')\rangle = \langle G_p(\mathbf{r},\mathbf{r}_0)\rangle\langle G_p^*(\mathbf{r}',\mathbf{r}_0')\rangle + \int \mathrm{d}\mathbf{r}_1\mathbf{r}_1'\langle G_p(\mathbf{r},\mathbf{r}_1)\rangle$$
$$\times\langle G_p^*(\mathbf{r}',\mathbf{r}_1')\rangle\langle V_p(\zeta(x_1))V_p(\zeta(x_1'))\rangle\langle G_p(\mathbf{r}_1,\mathbf{r}_0)\rangle\langle G_p^*(\mathbf{r}_1',\mathbf{r}_0')\rangle \tag{26}$$

The second term in the right-side of the above equation gives the first-order solution for the incoherent intensity $\Gamma_{incoh}^{(1)}(\kappa,q)$, which can be derived in using the coordinate transformation shown in Fig. 4, and after cumbersome manipulations.

As a special case, we let the source points $\mathbf{r}_0 = \mathbf{r}_0'$ and the observation points $\mathbf{r} = \mathbf{r}'$; this given the incoherent intensity at $\mathbf{r}$ due to the point source $\mathbf{r}_0$. We can express the cross section per unit length of the rough surface as [10]

$$\sigma_{h1}^{ESPM}(\kappa,q) = \frac{4}{k_0}\frac{k_z^2(\kappa)k_z^2(q)\tilde{W}(q-\kappa)}{|1+\Delta_{h1}(\kappa)|^2|1+\Delta_{h1}(q)|^2} \tag{27}$$

$$\sigma_{v1}^{ESPM}(\kappa,q) = \frac{4}{k_0}\frac{(k_0^2-\kappa\ q)\tilde{W}(q-\kappa)}{|1+\Delta_{v1}(\kappa)|^2|1+\Delta_{v1}(q)|^2} \tag{28}$$

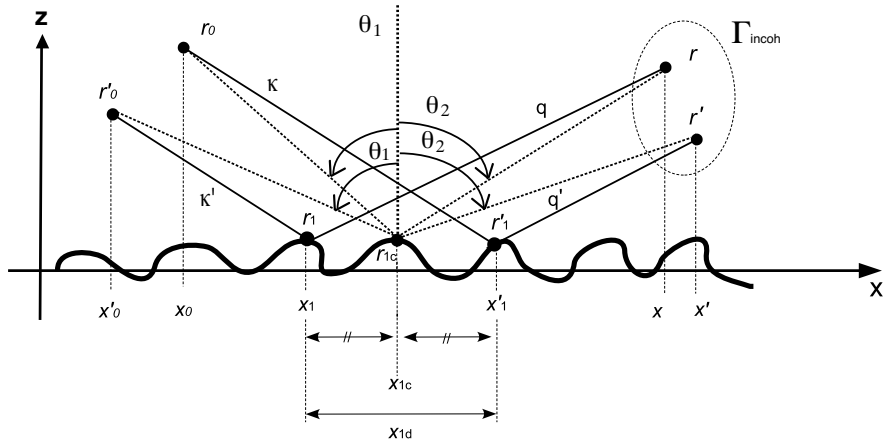

Figure 4. First-order incoherent function for the incoherent intensity of the Bethe-Salpeter equation. Dotted lines represent geometric coordinate relationship after the coordinate transformation.

where $\Delta_{h1}(\kappa) = \frac{k_z(\kappa)}{k_0} Z_{h1}(\kappa)$, $\Delta_{v1}(\kappa) = \frac{k_0}{k_z(\kappa)} Z_{v1}(\kappa)$. The couple $(\kappa = k_0 \sin\theta_1, q = k_0 \sin\theta_2)$ represents the wave numbers projected on x axis, of the incident field and scattered field at the point $\mathbf{r}_{1c}$ as shown in Fig. 3. The bistatic scattering coefficients of the first-order conventional perturbation method for both Dirichlet and Neumann cases, respectively, are [4]

$$\sigma_{h1}(\kappa, q) = \frac{4}{k_0} k_z^2(\kappa) k_z^2(q) \tilde{W}(q - \kappa) \tag{29}$$

$$\sigma_{v1}(\kappa, q) = \frac{4}{k_0} (k_0^2 - \kappa\, q)^2 \tilde{W}(q - \kappa) \tag{30}$$

The second-order bistatic scattering coefficients for co-polarization terms are [16]

$$\sigma_{p2}(\kappa, q) = \frac{k_z^2(\kappa)}{k_0} \Re e \left\{ \int \mathrm{d}\kappa' \tilde{W}(q - \kappa') \tilde{W}(\kappa' - \kappa) \right. \\ \left. \left[|A_p(q, \kappa')|^2 + A_p(q, \kappa') A_p^*(q, -\kappa' + q + \kappa) \right] \right\} \tag{31}$$

where $p = h, v$ and

$$A_p(q, \kappa') = \begin{cases} 2k_z(\kappa) k_z(\kappa') & \text{for } p = h \\ \dfrac{2}{k_z(q) k_z(\kappa')} \left(k_0^2 - q\kappa'\right) \left(\kappa'\kappa - k_0^2\right) & \text{for } p = v \end{cases} \tag{32}$$

We then get the general bistatic scattering coefficients of the Small Perturbation Method up to second-order

$$\sigma_{p(1-2)}^{SPM}(\kappa, q) = \sigma_{p1}(\kappa, q) + \sigma_{p2}(\kappa, q) \tag{33}$$

Also, we can give the following general form of the bistatic scattering coefficient based on the Extended Small Perturbation Method in term of the conventional one

$$\sigma_{p1}^{ESPM}(\kappa, q) = \sigma_{p1}^{SPM}(\kappa, q)|F_{p1}(\kappa)|^2|F_{p1}(q)|^2 \tag{34}$$

where the superscript ESPM stands for Extended Small Perturbation Method and $|F_{p1}(\kappa)|^2$ and $|F_{p1}(q)|^2$ are given in (27) and (28).

3. NUMERICAL RESULTS

3.1. Gaussian Spectrum

We assume the height spectrum to be Gaussian, such that

$$\tilde{W}(\kappa) = \frac{\sigma_h^2 l_c}{2\sqrt{\pi}} e^{-\frac{\kappa^2 l_c^2}{4}} \tag{35}$$

where l_c is the correlation length and σ_h is the RMS heights. This spectrum is usually used for optics applications. For our purpose it is convenient to introduce a more realistic spectrum to study the scattering of radio waves by a sea surface.

3.2. The Elfouhaily et al. Sea Spectrum

A reliable statistical description of wind-generated surface waves is of crucial importance for improving understanding of continuous motions and exchanges across the air-sea interface. Among statistical descriptions of waves, spectral formulation is generally stemming from the early work of Phillips [32].

It is recognized that for remote sensing studies, precise knowledge of the short-scale wave roughness is the prime requirement. As a first-order approximation, studies often present spectrum for only high wavenumbers. However it is now accepted that short-waves are intimately coupled with intermediate- and long-scale waves necessitating the need for full wavenumber models such those of *Donelan and Pierson* [33] and *Apel* [34], which can be used in modeling electromagnetic interactions with sea surface. These models are widely used in microwave radar scattering studies because of their attention to high-frequency spectral definition.

The omnidirectional spectrum is expressed as a sum of two spectra regimes:

$$\tilde{W}(\kappa) = \frac{B_l(\kappa) + B_h(\kappa)}{\kappa^3} \tag{36}$$

where subscripts l and h indicate low and high frequencies, and so B_l and B_h represent short and long waves contributions, respectively.

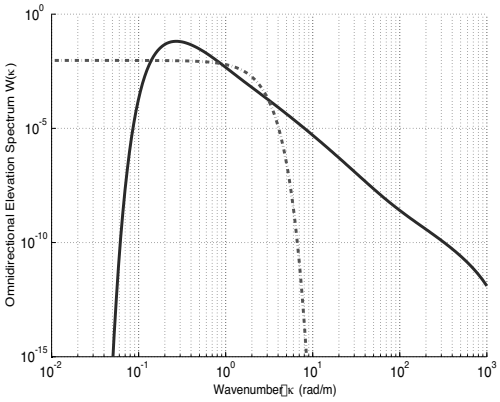

Figure 5. Gaussian (dashdot) and Elfouhaily heights spectra. Wind speed at a height of 10 m above the water surface: $U_{10} = 5\,\mathrm{m/sec}$. RMS heights $\sigma_h = 0.1609\,\mathrm{m}$ and RMS slopes $\sigma_s = 0.1767$.

In Fig. 5, gaussian and sea height spectra are plotted for a wind speed at 10 meters above the sea surface of $U_{10} = 5\,\mathrm{m/s}$. The RMS heights $\sigma_h = 0.1609\,\mathrm{m}$ and the RMS slopes $\sigma_p = 0.1767$. The RMS heights σ_h and the RMS slopes σ_p parameters are derived from the sea spectrum through

$$\sigma_h = \sqrt{\int_0^{+\infty} \tilde{W}(\kappa)\mathrm{d}\kappa} \tag{37}$$

$$\sigma_s = \sqrt{\int_0^{+\infty} \kappa^2 \tilde{W}(\kappa)\mathrm{d}\kappa} \tag{38}$$

and the correlation length $l_c = \frac{\sqrt{2}\sigma_h}{\sigma_s}$. These parameters are then implemented in the Gaussian spectrum (35). Another relevant parameter for the present study is the wavenumber of the spectral peak $K_p = \Omega^2 g/U_{10}^2$ where g is the acceleration due to gravity, and Ω the inverse wave age. In our example above, $K_p = 0.84^2 \times 9.81/5^2 = 0.2769\,\mathrm{rad/m}$. It can be readily verified in Fig. 5.

3.3. Numerical Simulations and Discussion

3.3.1. Effective Surface Impedance

We present numerical results for the dependance of the effective surface impedance on the incidence angle. In Figs. 6–9, we plot the real (resistive) and imaginary (reactive) parts of the first- and second-order effective surface impedance for the Dirichlet and Neumann cases respectively, versus the incidence angle, for the Gaussian and sea surfaces cases. The negative reactance for the Dirichlet case represents a capacitance and the positive one for the Neumann case represents an inductance.

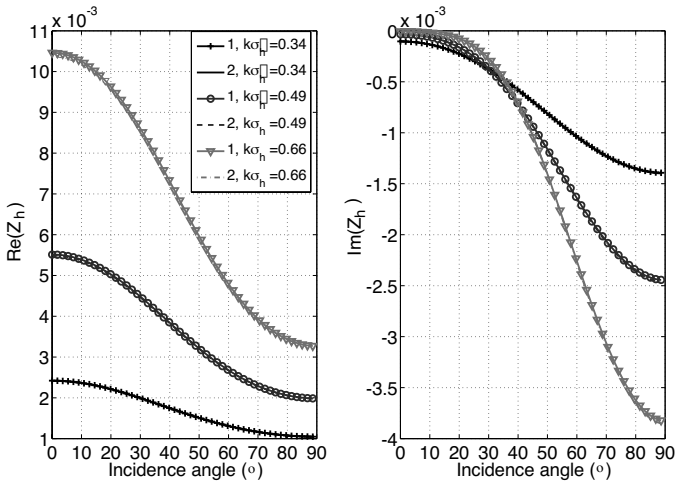

Figure 6. Real and imaginary parts of the effective surface impedance Z_h versus the angle of incidence for the Dirichlet boundary condition, for a Gaussian spectrum and for different parameters $k_0\sigma_h$. The solid curves are for the first-order surface impedance and the broken curves are for the second-order surface impedance. RMS heights $\sigma_h = \{0.16, 0.23, 0.32\}$ m, RMS slopes $\sigma_p = \{0.18, 0.19, 0.20\}$ and correlation lengths $l_c = \{1.3, 1.7, 2.2\}$ m., corresponding respectively to wind speeds $U_{10} = \{5, 6, 7\}$ m/s.

Figures 6–9 show that resistive components decrease with increasing angles of incidence, excepted for Neumann boundary condition in sea spectrum case. This tendency is more pronounced for larger values of $k_0\sigma_h$. Nevertheless, the reactive components for both spectra increase at the angles near grazing incidence.

Furthermore, at these angles, the enhancement of the second-order effective surface impedance, especially of the reactive component,

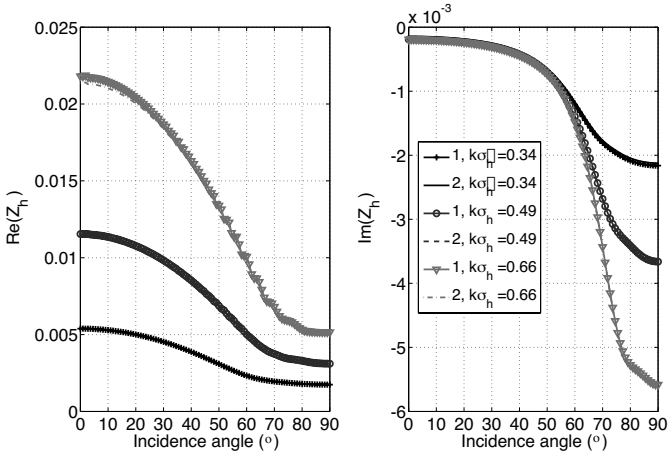

Figure 7. Same as in Fig. 6 but for a sea spectrum.

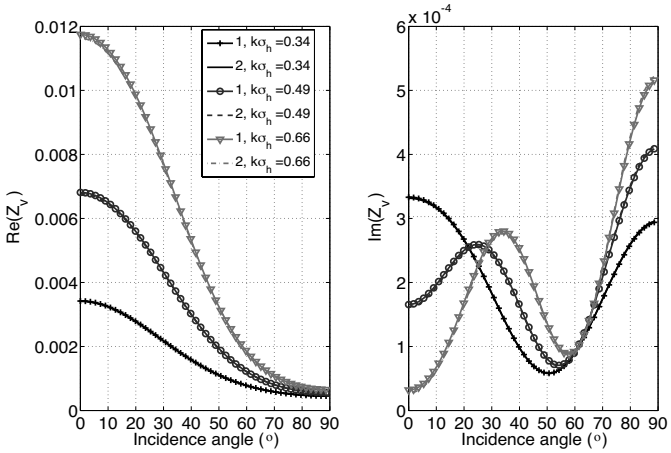

Figure 8. Same as Fig. 6, but for Neumann case.

occurs at $k_0\sigma_h$ becomes large. This would be due to the surface wave contribution, i.e., the contribution in (22) and (23) to the integral arises from the vicinity of the surface wave poles which lie very close to the real p_x axis. In the limiting case $k_0\sigma_h \to 0$, such enhancement does not occur since the surface impedance actually approaches zero.

As seen from (20) and (21), only roughness components whose spatial wavenumber is smaller than the incident wavenumber, i.e., $|\kappa| < k_0$, contribute to the resistive portion of the surface impedance

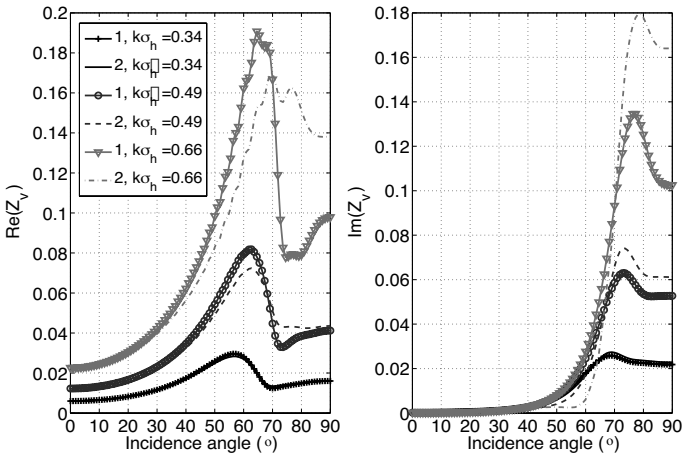

Figure 9. Same as Fig. 7, but for Neumann case.

and produce propagation waves (real k_z), which are scattered into the upper hemisphere. On the contrary, the remainder of the components, i.e., $|\kappa| > k_0$, contribute to the reactive portion and produce evanescent waves (imaginary k_z). These results are consistent with those obtained in [16] for a Gaussian spectrum and differ from the ones obtained from a sea spectrum.

The second order effective surface impedances (22) and (23) show that the roughness components $|\kappa| < k_0$ and $|\kappa| > k_0$ also contribute a decreasing in the reactive portion and an increasing in the resistive portion, respectively [13]. Physically, this suggests that the multiple interaction effect, due to surface roughness, gives rise to the energy transfer between evanescent modes and propagating modes.

In Figs. 10 and 11, we plotted the correction factors $|F_{p1}(\kappa)|^2$ from (34), both for Dirichlet and Neumann cases. The computation has been made for the same surface height spectrum as that used for the effective impedance surface.

For the Dirichlet case, the multiple scattering effect mainly appears for angles near zero but are not significant since the level of the correction factor is close to one, like the Neumann case. On the contrary, for the Neumann case the above effect is more pronounced as the angle of incidence becomes larger, yielding significant departure from the results obtained from the conventional SPM. This departure is more pronounced in the sea case, and it depends strongly of the RMS heights of the surface. Note that the dependence on $k_0\sigma_h$ and the angle of incidence for the Neumann case is very different from the Dirichlet case.

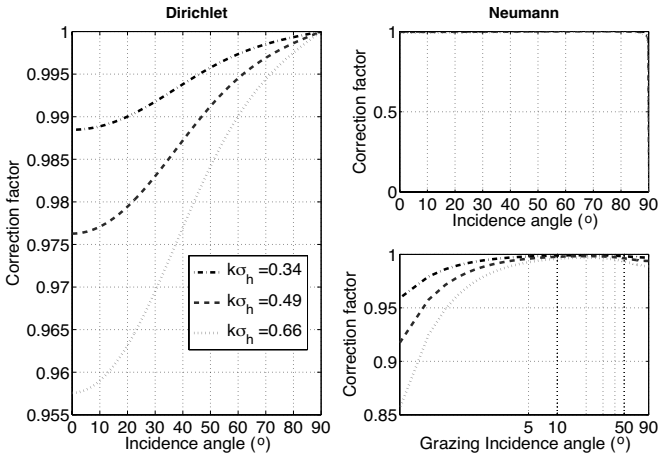

Figure 10. Dependance of the correction factor on angle of incidence for the Dirichlet boundary condition for a Gaussian spectrum. The correction to the SPM is obtained from the first-order correction in (27) and (28).

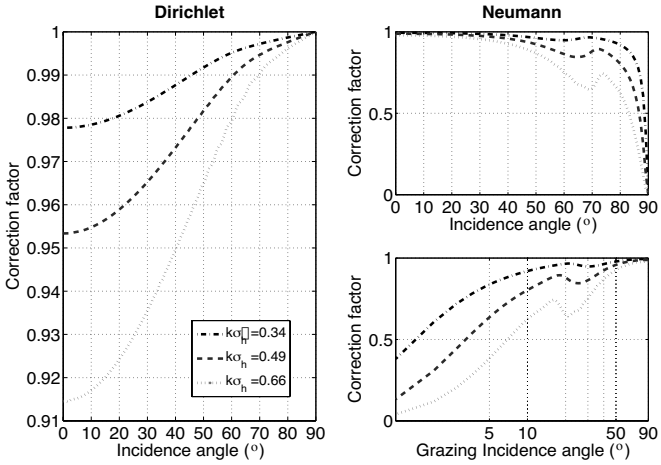

Figure 11. Same as Fig. 10, but for the sea spectrum case.

In Figs. 12 and 13, reflection coefficients, from the first-order surface impedance, are plotted. For a smooth Neumann surface, the Brewster-angle phenomenon does not occur. Nevertheless, we can observe that the modulus of reflection coefficient presents a local minimum near 90 degrees. By analogy with a smooth surface, this

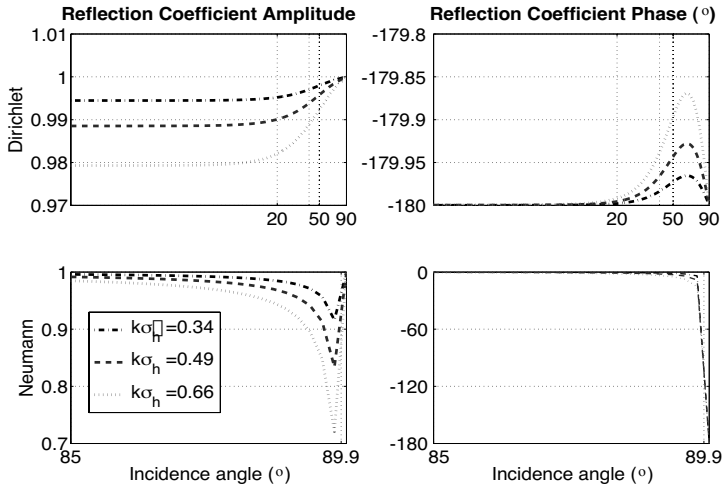

Figure 12. Amplitude and phase of the reflection coefficients for Dirichlet (on the top) and Neumann (on the bottom) boundary conditions, for a Gaussian spectrum.

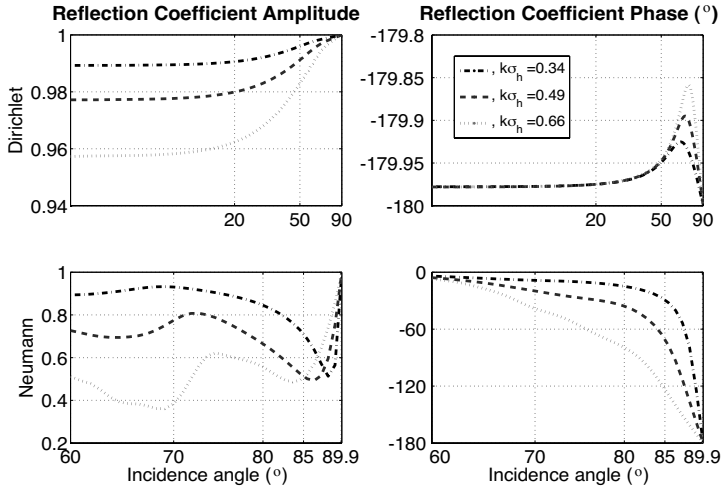

Figure 13. Same as Fig. 12, but for the sea spectrum case.

corresponds to the pseudo Brewster-angle phenomenon that occurs for a rough surface. In addition, as the roughness increases we note that this angle is shifted towards low angles and the associated value of the reflection coefficient decreases.

3.3.2. Bistatic Scattering Coefficients

For a Dirichlet rough surface and for Gaussian and sea spectra, the bistatic cross sections are plotted in Fig. 14 versus the observation angle. The wind speed is $U_{10} = 5\,\mathrm{m/s}$. The same variation is displayed in Fig. 15 but for the Neumann case.

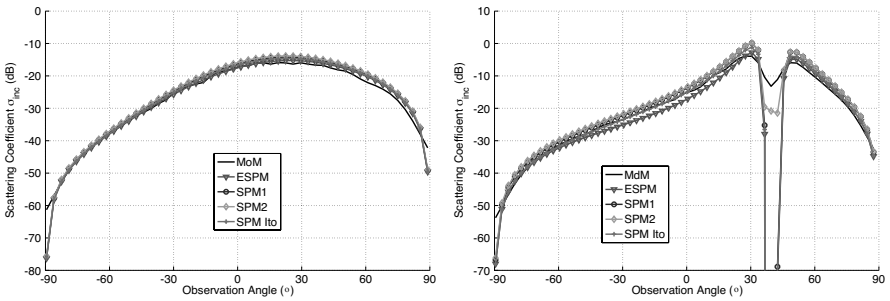

Figure 14. Comparison of the bistatic scattering coefficients $\sigma(\kappa, q)$ for the Dirichlet case. Incidence angle $\theta_i = 40°$. RMS heights $\sigma_h = 0.16\,\mathrm{m}$. The correlation length $l_c = 1.3\,\mathrm{m}$. MoM solution (solid curve), Extended SPM (triangle curve), first-order conventional SPM (circle curve), second-order conventional SPM (diamond curve), Itô's SPM solution (plus curve). On the left, Gaussian spectrum. On the right, sea spectrum.

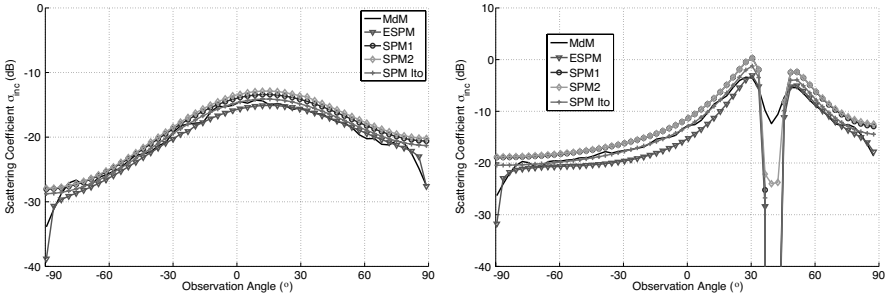

Figure 15. Same variation as in Fig. 14 but for the Neumann case.

The fall-off occurring in first-order conventional SPM solution at observation angle $\theta = 40^{\mathrm{o}}$, which is the specular direction, is due to the sea spectrum $\tilde{W}(q - \kappa)$ in Eqs. (27)–(34). Indeed, in the specular direction, $\kappa = q$, and, as shown in Fig. 5, leading that the corresponding elevation spectrum is zero. It is not the case in the benchmark solution since the height profile is generated with a

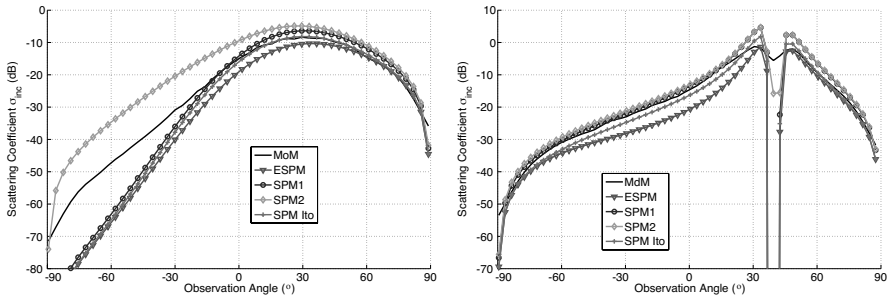

Figure 16. Same variation as in Fig. 14 but for a wind speed $U_{10} = 7\,\mathrm{m/s}$ (on the left) and $U_{10} = 6\,\mathrm{m/s}$ (on the right).

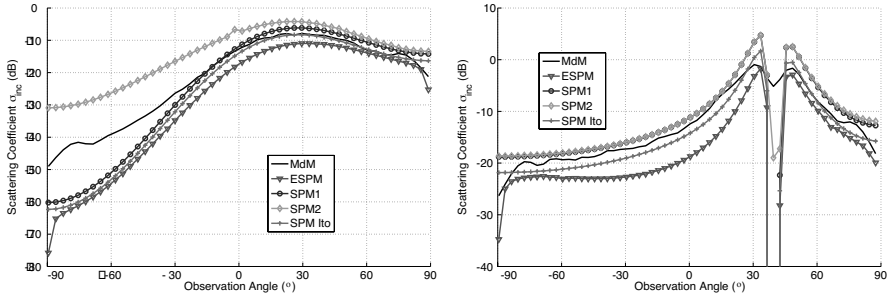

Figure 17. Same variation as in Fig. 16 but for the Neumann case.

minimum wavenumber value $\kappa_{\min} = 0.15K_p$, for which the elevation spectrum is small, but not zero.

In Figs. 16 and 17, the same variation is represented as in Figs. 14 and 15, but for $U_{10} = 7\,\mathrm{m/s}$ (gaussian spectrum) and $U_{10} = 6\,\mathrm{m/s}$ (sea spectrum).

The benchmark solution is obtained from the conventional Method of Moments (MoM), which is used as reference in many studies [21–25]. The surface length is 100λ, the sampling step $\Delta x = 0.1\lambda$, the Thorsos's incident wave is characterized by $g = L/6$. The number of Monte Carlo realizations is 100 [26]. The frequency is $f = 100\,\mathrm{MHz}$ and $\lambda = 3\,\mathrm{m}$.

In Figs. 16 and 17 for a sea spectrum the wind speed is $U_{10} = 6\,\mathrm{m/s}$, since beyond $k_0\sigma_h = 0.49$, both conventional SPM and Extended SPM failed. That is not true with the Gaussian spectrum case.

For small RMS height $k_0\sigma_h \leq 0.25$ (not presented), all bistatic scattering coefficients are approximately equivalent. As $k_0\sigma_h$ increases,

the results obtained by conventional perturbation solution increases faster than the extended one, which gives good agreement. The later is however below the reference values, and, actually, it is expected that the higher order solutions of the ESPM should be increased the level in order to reach in a better way the reference solution. To our knowledge, no calculation has been published on this issue. Indeed, higher orders need much more cumbersome mathematical handling. As well, it should be expected that the higher order of conventional SPM solution would contribute a decreasing in power. It is readily clear for the Gaussian case at $k_0\sigma_h = 0.66$ ($U_{10} = 7\,\mathrm{m/s}$), that there is a departure of the second-order SPM solution in backscattering direction. However, the sea case does not show this behavior for the second-order SPM solution since both first- and second-orders are quite in agreement, even if $k_0\sigma_h = 0.49$ ($U_{10} = 6\,\mathrm{m/s}$) in this case.

The Itô first-order solution [13], based on the assumption corresponding to the diagrammatic form of the Bethe-Salpeter equation shown in Fig. 3(c), is identical to the Watson-Keller formula [27] which is not reciprocal. However, (27) and (28) are reciprocal leading to

$$\sigma(\kappa, q) = \sigma(-q, -\kappa) \tag{39}$$

Equations (27) and (28) satisfied the reciprocity condition since the height spectrum is an even function. In addition, from the first-order perturbation theory, we take into account not only the resonant Bragg scattering via the term $\tilde{W}(q - \kappa)$ in Eqs. (27) and (28), but also the attenuation of the incident wave due to multiple scattering processes via the correction factor $|F_{p1}|^2$. The scattered wave then propagates from x_{1c} in q-direction including rough surface effects.

4. CONCLUDING REMARKS

In this paper, the multiple scattering theory developed by Bass et al. is studied to predict the scattering from a one-dimensional perfectly-conducting Gaussian rough sea surface of the Gaussian and the more realistic Elfouhaily et al. spectra. Theoretically, this asymptotic solution for the intensity of incoherent waves shows that the multiple scattering effect is incorporated into the solution in terms of the effective surface impedance. This leads to bring a correction to the usual SPM of Rice.

The main contribution of this work is the presentation of numerical results for two height spectra. We first plotted the behavior of the effective surface impedances for both spectra. From these surface impedances, we displayed the reflection coefficients which exhibit,

in TM case, a pseudo Brewster-angle phenomenon, well-known for non perfectly-conducting smooth surfaces. Then, the numerical investigations of the bistatic scattering coefficient for both Neumann and Dirichlet boundary conditions, for a rough sea surface, obeying to the Elfouhaily et al. spectrum, in HF-VHF band, show good agreement between the theory and the benchmark method.

However, as discussed earlier, numerical results for the correction factor show that the ESPM provides a relatively good result for Dirichlet case, while it is not valid at near-grazing incidence for Neumann case, since Figs. 10–11 show a significant departure. The latter case indicates a definite need as grazing incidence approach. It is for example the purpose of the paper [28], based on the results of Barrick [20], the paper [29] which derives a new Grazing Perturbation (GP), or [30] where authors make use of the Parabolic Wave Equation to take into account interaction phenomena of the wave with propagation media. For this goal, accelerated benchmark solution are necessary [31].

This study is relevant for application in remote sensing for coastal radar for example. Actually, it will lead to the real case, a finitely conducting rough sea surface, which will be the purpose in a future paper, as well as study at grazing angle under the formulation presented in this paper.

APPENDIX A. EVALUATION OF THE INTEGRAL OF THE TM EFFECTIVE SURFACE IMPEDANCE $Z_{V1}(\kappa)$

This appendix presents a way to remove the pole, which occurs in the integrand of effective surface impedance for the TM case (Eq. (21)), given by

$$Z_{v1}(\kappa) = \int_{-\infty}^{+\infty} \frac{\mathrm{d}\kappa'}{k_0 k_z(\kappa')} (k_0^2 - \kappa\kappa')^2 \tilde{W}(\kappa - \kappa') \tag{A1}$$

Writing $Z_{v1}(\kappa) = \alpha_{v1}(\kappa) + j\beta_{v1}(\kappa)$, we obtain from (21)

$$\begin{cases} \alpha_{v1}(\kappa) = \displaystyle\int_{-k_0}^{+k_0} \frac{\mathrm{d}\kappa'}{k_0\sqrt{k_0^2 - \kappa'^2}} (k_0^2 - \kappa\kappa')^2 \tilde{W}(\kappa - \kappa') \\ \beta_{v1}(\kappa) = -\displaystyle\int_{-\infty}^{-k_0} \frac{\mathrm{d}\kappa'}{k_0\sqrt{-\kappa'^2 - k_0^2}} (k_0^2 - \kappa\kappa')^2 \tilde{W}(\kappa - \kappa') \\ \qquad\qquad -\displaystyle\int_{k_0}^{\infty} \frac{\mathrm{d}\kappa'}{k_0\sqrt{-\kappa'^2 - k_0^2}} (k_0^2 - \kappa\kappa')^2 \tilde{W}(\kappa - \kappa') \end{cases} \tag{A2}$$

For $\kappa' = \pm k_0$, the denominator of the integrand vanishes, implying that the integrand diverges. In order to remove this effect, we use a variable transformation.

For convenience, we can split the real part $\alpha_{v1}(\kappa)$ as

$$\begin{aligned}\alpha_{v1}(\kappa) &= \int_{-k_0}^{0} \frac{\mathrm{d}\kappa'}{k_0\sqrt{k_0^2 - -\kappa'^2}}(k_0^2 - \kappa\kappa')^2\tilde{W}(\kappa - \kappa') \\ &\quad + \int_{0}^{k_0} \frac{\mathrm{d}\kappa'}{k_0\sqrt{k_0^2 - -\kappa'^2}}(k_0^2 - \kappa\kappa')^2\tilde{W}(\kappa - \kappa') \qquad \text{(A3)}\end{aligned}$$

Noting that $\sqrt{k_0^2 - -\kappa'^2} = \sqrt{(k_0 - \kappa')(k_0 + \kappa')}$, we make a variable transformation $u_1 = \sqrt{k_0 + \kappa'}$ (the pole is $\kappa' = -k_0$) for the first integral in Eq. (A3) and $u_2 = \sqrt{k_0 - \kappa'}$ (the pole is $\kappa' = +k_0$) in the second integral of (A3). This leads to the following result

$$\begin{aligned}\alpha_{v1}(\kappa) &= \sum_{s=\pm}\int_{0}^{\sqrt{k_0}} \frac{\mathrm{d}u}{k_0\sqrt{-u^2 + 2k_0}} \\ &\quad \times \left[k_0^2 + s\kappa\left(k_0 - u^2\right)\right]^2 \tilde{W}\left(\kappa + s\left[k_0 - u^2\right]\right) \qquad \text{(A4)}\end{aligned}$$

We now let consider the imaginary part $\beta_{v1}(\kappa)$

$$\begin{aligned}\beta_{v1}(\kappa) &= -\int_{-\infty}^{-k_0} \frac{\mathrm{d}\kappa'}{k_0\sqrt{-\kappa'^2 - k_0^2}}(k_0^2 - \kappa\kappa')^2\tilde{W}(\kappa - \kappa') \\ &\quad - \int_{k_0}^{\infty} \frac{\mathrm{d}\kappa'}{k_0\sqrt{-\kappa'^2 - k_0^2}}(k_0^2 - \kappa\kappa')^2\tilde{W}(\kappa - \kappa') \qquad \text{(A5)}\end{aligned}$$

The limit of integration in the first integral of Eq. (A5) can be expressed in the same way as the second one by making the transformation $\kappa' \to -\kappa'$. We then let $u = \sqrt{-\kappa'^2 - k_0^2}$, leading to the substitution of the pole $\sqrt{-\kappa'^2 - k_0^2}$ by $\sqrt{u^2 + k_0^2}$ where the variable u ranges from 0 to $+\infty$. As for the real part, we can express the imaginary part in the following manner

$$\begin{aligned}\beta_{v1}(\kappa) &= -\sum_{s=\pm}\int_{0}^{+\infty} \frac{\mathrm{d}u}{k_0\sqrt{k_0^2 + u^2}} \\ &\quad \times \left[k_0^2 + s\kappa\sqrt{k_0^2 + u^2}\right]^2 \tilde{W}\left(\kappa + s\sqrt{k_0^2 + u^2}\right) \qquad \text{(A6)}\end{aligned}$$

It can then be readily verified that no pole of the integrand of $Z_{v1}(\kappa)$ is crossed or approached. It is also interesting to notify that for the real part of Eq. (21), for a Gaussian height spectrum (35) and $\kappa = 0$ (normal incidence angle), the integral is expressed in a closed-form as follows

$$\alpha_{v1}(\kappa) = \xi\sigma_h^2 k_0^2 \sqrt{\pi} e^{-\frac{\xi^2}{2}} I_0\left(\frac{\xi^2}{2}\right) \tag{A7}$$

where I_0 is the modified Bessel function of first kind and zeroth order, and $\xi = k_0 l_c/2$.

REFERENCES

1. Beckmann, P. and A. Spizzichino, *The Scattering of Electromagnetic Waves from Rough Surfaces*, Pergamon, New York, 1963.
2. Rice, S. O., "Reflection of electromagnetic waves from slightly rough surfaces," *Theory of Electromagnetic Waves*, edited by Kline, M., 351–378, Interscience, New York, 1951.
3. Fuks, I. M. and F. G. Bass, *Wave Scattering for Statistically Rough Surfaces*, Pergamon, New York, 1979.
4. Voronovich, A. G., *Wave Scattering from Rough Surface*, Spring-Verlag, Berlin, 1994.
5. Berginc, G. and C. Bourrely "The small-slope approximation method applied to a three-dimensional slab with rough boundaries," *Progress in Electromagnetic Research*, PIER 73, 131–211, 2007.
6. Ishimaru, A., *Wave Propagation and Scattering in Random Media*, Academic, New York, 1978.
7. Tsang, L. and J. A. Kong, *Scattering of Electromagnetic Waves: Theories and Applications*, Vol. 1, Wiley-Interscience, New York, 2001.
8. Fuks, I. M., "Correction to asymptotic solutions for backscattering by smooth 2D surfaces," *Journal of Electromagnetic Waves and Applications*, Vol. 20, No. 14, 2103–2103, 2006.
9. Mudaliar, S., "On the application of the radiative transfer approach to scattering from a random medium layer with rough boundaries," *Journal of Electromagnetic Waves and Applications*, Vol. 20, No. 13, 1739–1749, 2006.
10. Fuks, I. M., V. I. Tatarskii, and D. E. Barrick, "Behavior of scattering from a rough surface at small grazing angles," *Wave in Random Media*, No. 9, 295–305, 1999.

11. Ishimaru, A., J. D. Rockway, and Y. Kuga, "Rough surface Green's function based on the first-order modified perturbation and smoothed diagram methods," *Wave in Random Media*, Vol. 10, 17–31, 2000.
12. Feinberg, E., "On the propagation of radio waves along an imperfect surface," *Journal of Physics*, Vol. 8, No. 6, 317–330, 1944.
13. Itô, S., "Analysis of scalar wave scattering from slightly rough random surfaces: A multiple scattering theory," *Radio Science*, Vol. 20, No. 1, 1–12, 1985.
14. Elfouhaily, T., B. Chapron, and K. Katsaros, "A unified directional spectrum for long and short wind-driven waves," *Journal of Geophysical Research*, Vol. 102, No. C7, 15781–15796, 1997.
15. Frisch, U., "Wave propagation in random media," *Probabilistic Methods in Applied Mathematics*, A. T. Bharucha-Reid (ed.), 75–198, Academic, New York, 1968.
16. Tsang, L. and J. A. Kong, *Scattering of Electromagnetic Waves: Advanced Topics*, Vol. 3, Wiley-Interscience, New York, 2001.
17. Ogura, H. and N. Takahashi, "Scattering, radiation and propagation over two-dimensional random surface," *Progress in Electromagnetic Research*, PIER 14, 89–180, 1996.
18. Fung, A. K. and N. C. Kuo, "Backscattering from multi-scale and exponentially correlated surfaces," *Journal of Electromagnetic Waves and Applications*, Vol. 20, No. 1, 3–11, 2006.
19. Chen, K. S., A. K. Fung, J. C. Shi, and H. W. Lee, "Interpretation of backscattering mechanisms from non-Gaussian correlated randomly rough surfaces," *Journal of Electromagnetic Waves and Applications*, Vol. 20, No. 1, 105–118, 2006.
20. Barrick, D. E., "Theory of HF and VHF propagation across the rough sea, I and II," *Radio Science*, Vol. 6, No. 5, 517–533, 1971.
21. Huang, E. X. and A. K. Fung, "An application of sampling theorem to moment method simulation in surface scattering," *Journal of Electromagnetic Waves and Applications*, Vol. 20, No. 4, 531–546, 2006.
22. Zhang, Y., J. Wang, Z. Zhao, and J. Yang, "The analysis of LPDA using MOM and transmission matrix," *Journal of Electromagnetic Waves and Applications*, Vol. 21, No. 12, 1621–1633, 2007.
23. Zou, Y., Q. Liu, and J. Guo, "Fast analysis of body-of-revolution radomes with Method of Moments," *Journal of Electromagnetic Waves and Applications*, Vol. 21, No. 13, 1803–1817, 2007.

24. Papakanellos, P. J., "Alternative sub-domain Moment Methods for analyzing thin-wire circular loops," *Progress in Electromagnetic Research*, PIER 71, 1–18, 2007.
25. Wang, S., X. Guan, D. Wang, X. Ma, and Y. Su "Electromagnetic scattering by mixed conducting/dielectric objects using higher-Order MOM," *Progress in Electromagnetic Research*, PIER 66, 51–63, 2006.
26. Mishra, M. and N. Gupta, "Monte Carlo integration technique for the analysis of electromagnetic scattering from conducting surfaces," *Progress in Electromagnetic Research*, PIER 79, 91–106, 2008.
27. Watson, J. G. and J. B. Keller, "Reflection, scattering and absorption of acoustic waves by rough surfaces," *Journal of the Acoustical Society of America*, Vol. 74, No. 6, 1887–1894, 1983.
28. Fabbro, V., P. F. Combes, and N. Guillet, "Apparent radar cross section of a large target illuminated by a surface wave above the sea," *Progress In Electromagnetic Research*, PIER 50, 41–60, 2005.
29. Charnotskii, M. I., "Wave scattering by periodic surface at low grazing angles: Single grazing mode," *Progress In Electromagnetic Research*, PIER 26, 1–41, 2000.
30. Fabbro, V., C. Bourlier, and P. F. Combes, "Forward propagation modeling above Gaussian rough surfaces by the Parabolic shadowing effect," *Progress in Electromagnetic Research*, PIER 58, 243–269, 2006.
31. Xu, L., Y. C. Guo, and X. W. Shi, "Dielectric half space model for the analysis of scattering from objects on ocean surface," *Journal of Electromagnetic Waves and Applications*, Vol. 21, No. 15, 2287–2296, 2007.
32. Phillips, O. M., "The equilibrium range in the spectrum of wind generated waves," *Journal of Fluid Mechanics*, Vol. 4, 426–434, 1958.
33. Donelan, M. A., and W. J. P. Pierson, "Radar scattering and equilibrium ranges in wind-generated waves with application to scatterometry," *Journal of Geophysical Research*, Vol. 92, 4971–5029, 1987.
34. Apel, J. R., "An improved model of the ocean surface wave vector spectrum and it effects on radar backscatter," *Journal of Geophysical Research*, Vol. 99, 16269–16291, 1994.